Reflectivity calculated for a three-dimensional silicon photonic band gap crystal with finite support

D. Devashish,[1,2,*] Shakeeb B. Hasan,[1,†] J. J. W. van der Vegt,[2,‡] and Willem L. Vos[1,§]
[1]*Complex Photonic Systems (COPS), MESA+ Institute for Nanotechnology, University of Twente, P.O. Box 217, 7500 AE Enschede, The Netherlands*
[2]*Mathematics of Computational Science (MACS), MESA+ Institute for Nanotechnology, University of Twente, P.O. Box 217, 7500 AE Enschede, The Netherlands*
(Received 5 September 2016; revised manuscript received 21 February 2017; published 26 April 2017)

We study numerically the reflectivity of three-dimensional (3D) photonic crystals with a complete 3D photonic band gap. We employ the finite element method to study crystals with the cubic diamondlike inverse woodpile structure. The high-index backbone has a dielectric function similar to silicon. We study crystals with a range of thicknesses up to ten unit cells ($L \leqslant 10c$). The crystals are surrounded by vacuum, and have a finite support as in experiments. The polarization-resolved reflectivity spectra reveal Fabry-Pérot fringes related to standing waves in the finite crystal, as well as broad stop bands with nearly 100% reflectivity, even for thin crystals. The frequency ranges of the stop bands change little with angle of incidence, which is plausible since the stop bands are part of the 3D band gap. Moreover, this result supports the previous assertion that intense reflection peaks measured with a large numerical aperture provide a faithful signature of the 3D photonic band gap. For p-polarized waves, we observe an intriguing hybridization between the Fabry-Pérot resonances and the Brewster angle that remains to be observed in experiments. From the strong reflectivity peaks, it is inferred that the maximum reflectivity observed in experiments is not limited by finite size. The frequency ranges of the stop bands agree very well with stop gaps in the photonic band structure that pertain to infinite and perfect crystals. The angle-dependent reflectivity spectra provide an improved interpretation of the reflectivity measurements performed with a certain numerical aperture and a new insight in the crystal structure, namely unequal pore radii in X and Z directions. The Bragg attenuation lengths L_B are found to be smaller by a factor 6 to 9 than earlier estimates that are based on the width of the stop band. Hence, crystals with a thickness of 12 unit cells studied in experiments are in the thick crystal limit ($L \gg L_B$). Our reflectivity calculations suggest that the 3D silicon photonic band gap crystals are interesting candidates for back reflectors in a solar cell in order to enhance the photovoltaic efficiency.

DOI: 10.1103/PhysRevB.95.155141

I. INTRODUCTION

There is a worldwide interest in three-dimensional (3D) photonic crystals that radically control both the propagation and the emission of light [1–8]. Their application includes controlling spontaneous emission of embedded quantum emitters [9–12] and cavity quantum electrodynamics (QED) [13], controlling thermal emission [14,15], realizing efficient miniature lasers [16], efficient photoelectric conversion in solar cells [17], and cloaking [18]. In photonic crystals the refractive index varies spatially with a periodicity on length scales comparable to the wavelength of light. Due to the long-range periodic order, the photonic dispersion relations are organized in bands, analogous to electron bands in a semiconductor [19]. Light cannot propagate in a certain direction when the frequency is in a stop gap, as a result of Bragg diffraction [19]. Of prime significance to photonic crystals is the emergence of a 3D photonic band gap, a frequency range for which light is forbidden for all wave vectors and all polarizations [2,3,7]. A 3D photonic crystal is potentially a perfect back reflector in a solar cell to enhance the distance light travels through internal reflections [20].

The experimental demonstration of a 3D photonic band gap remains a major challenge. By definition, a 3D band gap corresponds to a frequency range where the density of optical states (DOS) vanishes. To probe the DOS, spectra or dynamics are studied of emitters positioned inside the crystal [9–12]. Such experiments are difficult and require sources as well as detection methods. On the other hand, a band gap is indicated by the overlap of stop bands for all directions of incidence, as shown by a peak in reflectivity or a trough in transmission [21–27] for ideally all directions. A peak in reflectivity or a trough in transmission may also occur, however, when incident waves do not couple to a field mode inside the crystal [7,28,29]. Thus, experimentally observed stop bands are typically interpreted by comparing to stop gaps calculated from band structures. As band structures pertain only to infinite and perfect crystals, features related to finite size or to unavoidable deviations from perfect periodicity are not considered.

Recently, several experimental studies of powerful silicon woodpile and silicon inverse woodpile photonic crystals were reported [26,27,30]. In these three studies, a maximum reflectivity was found in the range from 40% to 60%, and the deviations from ideal 100% were attributed to various reasons, mostly experimental ones. It was asserted that intense reflection peaks measured with a large numerical aperture provide a faithful signature of the 3D photonic band gap. The limited reflectivity was attributed to the limited crystal thickness in comparison to the Bragg attenuation length and to surface roughness, although no theoretical or numerical support was offered for these notions.

*d.devashish@utwente.nl
†s.b.hasan@utwente.nl
‡j.j.w.vandervegt@utwente.nl
§w.l.vos@utwente.nl

Therefore, in the present article, we study numerically the reflectivity of 3D photonic band gap crystals. We apply the finite element method to calculate reflectivity of crystals with the cubic diamondlike inverse woodpile structure that have a broad 3D photonic band gap [31–33]. Inverse woodpile photonic crystals have been realized in several different backbone materials using various techniques [34–37]. Our research group has fabricated 3D inverse woodpile photonic crystals from silicon using several CMOS-compatible methods [38–40]. The high-index backbone of the crystals has a dielectric function similar to silicon. We investigate crystals with thicknesses up to ten unit cells. Since the crystals are surrounded by vacuum, they have a finite support as in the experiments. We assess previously invoked limitations to the reflectivity, such as crystal thickness, angle of incidence, and Bragg attenuation length. Consequently, our numerical study provides an improved interpretation of reflectivity as a signature of a complete 3D photonic band gap.

II. METHODS

The primitive unit cell of the cubic inverse woodpile photonic structure is illustrated in Fig. 1. The crystal structure consists of two 2D arrays of identical pores with radius r running in two orthogonal directions X and Z [31]. Each 2D array has a centered-rectangular lattice with lattice parameters c and a. When the lattice parameters have a ratio $\frac{a}{c} = \sqrt{2}$, the diamondlike structure is cubic. In terms of the conventional

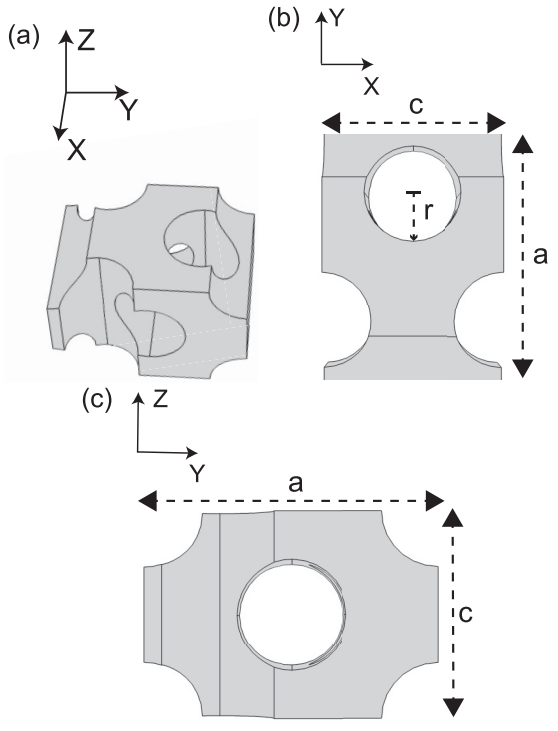

FIG. 1. The tetragonal primitive unit cell of the cubic inverse woodpile photonic crystal structure. (a) Perspective view of the unit cell with the XYZ coordinate system. The two sets of pores are parallel to the X and the Z axes. (b) View of the unit cell along the Z axis with the lattice parameters a and c and the pore radius r. (c) View of the unit cell along the X axis.

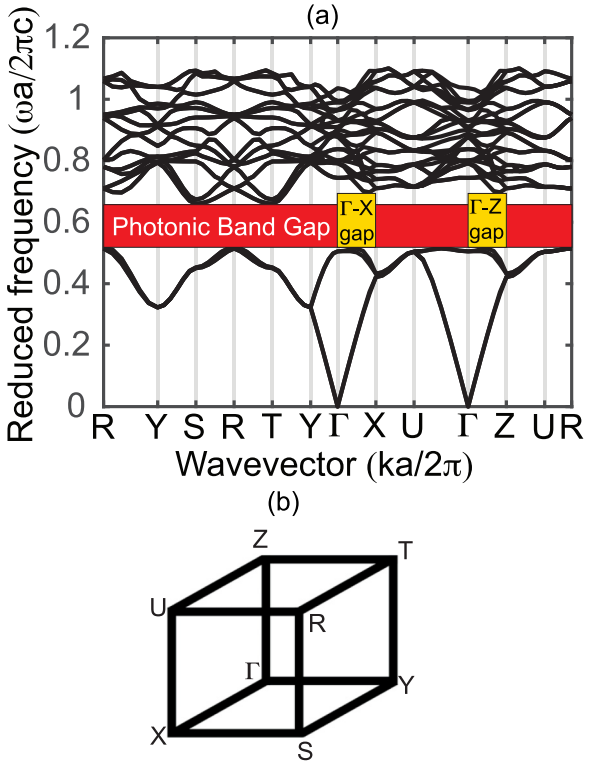

FIG. 2. (a) Photonic band structure for the 3D inverse woodpile photonic crystal with $\frac{r}{a} = 0.245$ and $\epsilon_{\mathrm{Si}} = 11.68$. The red bar marks the 3D photonic band gap, and the yellow bars mark stop gaps in the ΓX and ΓZ directions. (b) First Brillouin zone showing the high symmetry points and the origin at Γ.

nonprimitive cubic unit cell of the diamond structure, the (X,Y,Z) coordinate system shown in Fig. 1(a) has the X-axis unit vector $a_1 = \frac{1}{\sqrt{2}}[101]$, the Y-axis $a_2 = [010]$, and the Z-axis $a_3 = \frac{1}{\sqrt{2}}[\bar{1}01]$ in the coordinate frame of the conventional cubic unit cell [19]. Cubic inverse woodpile photonic crystals with $\epsilon = 11.68$ [41]—typical of silicon—have a broad maximum band gap width $\Delta\omega/\omega_c = 23.7\%$ relative to the central band gap frequency ω_c for pores with a relative radius $\frac{r}{a} = 0.245$ [32,33]. To compare our calculations with experimental results [39], we choose the pore radius to be $\frac{r}{a} = 0.19$ and the lattice parameter to be $a = 677$ nm [42]. To compute the dispersion relations for infinitely extended crystals, we employed the MPB plane-wave expansion method [43]. Figures 2(a) and 2(b) show the band structure and the first Brillouin zone for an inverse-woodpile crystal with optimal pore size $\frac{r}{a} = 0.245$. A broad photonic band gap with a 23.7% relative width appears between reduced frequency $\tilde{\omega}_1 = 0.52$ (bounded by the third and fourth bands) and $\tilde{\omega}_2 = 0.66$ (fifth band) [44]. The band structure shows two stop gaps in the ΓZ direction. Since the ΓX stop gap is symmetry related to the ΓZ stop gap, we effectively consider both stop gaps in the present study. The lowest-frequency narrow stop gap appears between $\tilde{\omega} = 0.421$ and $\tilde{\omega} = 0.433$ and closes when moving in the ZU direction. The second stop gap between $\tilde{\omega} = 0.52$ and $\tilde{\omega} = 0.70$ is part of the complete 3D photonic band gap and has a broad 29.5% relative bandwidth. In the low-frequency limit $\omega \to 0$, we derive from the slope

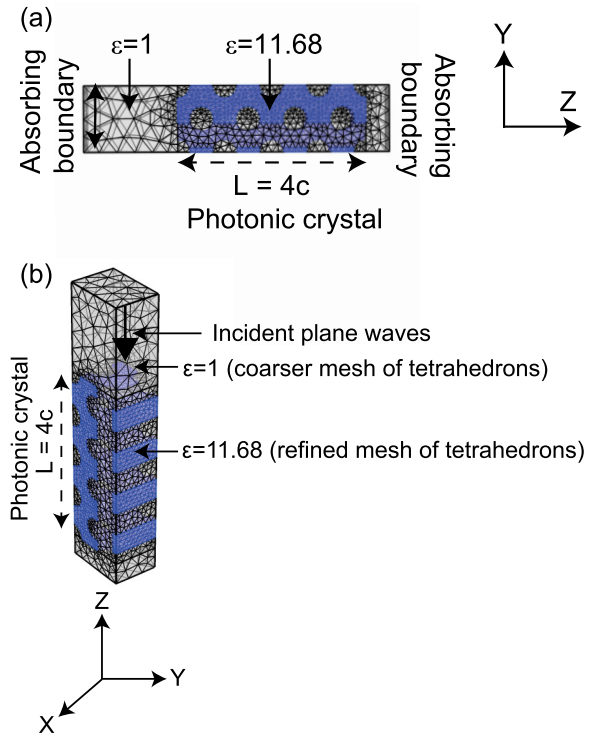

FIG. 3. Illustration of the computational cell for a photonic crystal with thickness $L = 4c$. (a) View along the X direction [101]. The source of plane waves is at the left, and is separated by an air layer from the crystal. The computational cell is bounded by absorbing boundaries at $-Z$ and $+Z$, and by periodic boundary conditions on $\pm X$ and $\pm Y$. The blue color represents the high-index backbone of the crystal having dielectric function similar to silicon. (b) Perspective view of the computational cell.

of the bands the effective refractive index of the crystal to be $n_e = 1.68$.

To accurately model the reflectivity and transmission spectra of photonic band gap crystals with finite support, we employ the commercial COMSOL finite-element (FEM) solver to solve for the time-harmonic Maxwell equations [45]. Figure 3(a) illustrates the computational cell along the X direction. The incident fields emanate from a plane at the left that is separated from the crystal by an air layer. The plane rather represents a boundary condition than a true current source since it also absorbs the reflected waves [46]. The incident plane waves have either s polarization (electric field normal to the plane of incidence) or p polarization (magnetic field normal to the plane of incidence), and have an angle of incidence between 0° and 80°. To mimic infinite space by minimizing the back reflections, absorbing boundaries are employed in the $-Z$ and $+Z$ directions, where the crystal is finite in size. We employ Bloch-Floquet periodic boundaries in the $\pm X$ and the $\pm Y$ directions to describe a crystal slab [7]. Figure 3(b) illustrates the finite element mesh used to subdivide the 3D computational cell. We used tetrahedra as basic elements in our finite element mesh. An upper limit of $\Delta l \leqslant \frac{\lambda_0}{8\sqrt{\epsilon}}$ is imposed to the edge length Δl on any tetrahedron, with λ_0 the shortest wavelength of the incident plane waves in vacuum, leading to a finite element mesh of 27 852 tetrahedra per unit cell. A refined mesh is used at the interface between the high-index material and the low-index material to reduce dispersion errors. For computational efficiency, we apply the MUMPS direct solver that is fast, multicore capable, and cluster capable. For a single frequency and a single angle of incidence, the computational time is 35 s on a Intel Core i7 machine with a single processor of four cores. We found that the computational time increases sublinearly with respect to the number of frequency steps and the number of angle of incidence steps.

III. RESULTS

A. Angle- and frequency-resolved reflectivity

Figure 4 shows the angle-resolved and frequency-resolved reflectivity spectra for an inverse-woodpile crystal with a thickness $L = 4c$ for angles of incidence up to 80° off normal and for optimal pore radius $\frac{r}{a} = 0.245$. Near $\tilde{\omega} = 0.6$ we observe broad stop bands with nearly 100% reflectivity for

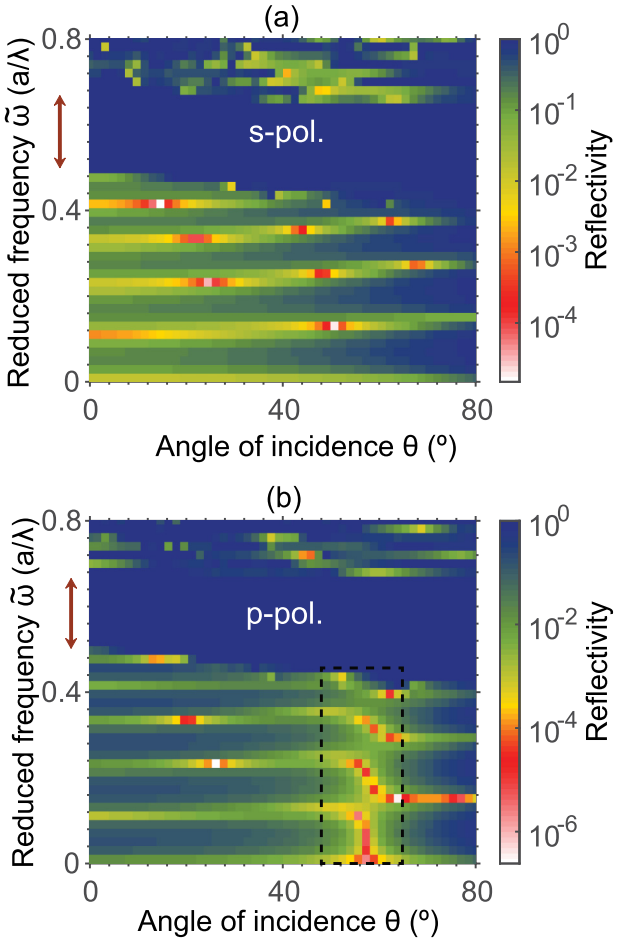

FIG. 4. Calculated angle- and frequency- resolved reflectivity spectra in the ΓZ direction for a crystal with thickness $L = 4c$ for (a) s polarization and (b) p polarization. The dark blue color represents high reflectivity that occurs in the stop band at all angles. The white color represents near 0% reflectivity that occurs in the Fabry-Pérot fringes, at the Brewster angle, and in their hybridization in the range $54° \leqslant \theta \leqslant 61°$. The brown double arrow represents the stop gap in the ΓZ direction (from Fig. 2). The black box indicates the region of high-resolution results shown in Fig. 5.

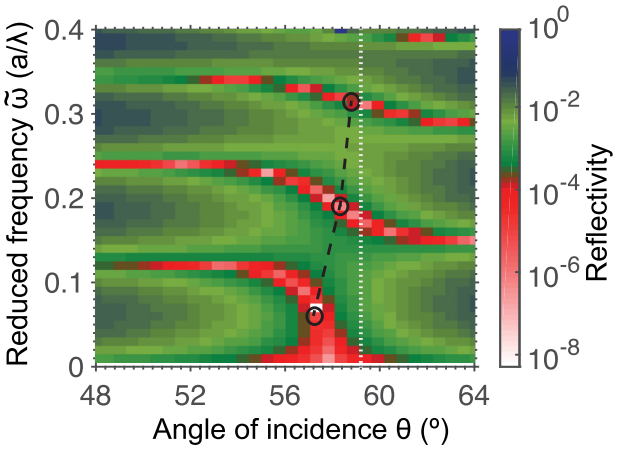

FIG. 5. Hybridization of the Fabry-Pérot resonances and the Brewster angle, shown by angle- and frequency- resolved calculated reflectivity spectra in ΓZ direction for p polarization. The black dashed line is a guide to the eye that connects the midpoints (circles) of the bends in the fringes. The white dotted line indicates the Brewster angle θ_B.

both polarizations. The stop bands agree very well with the stop gaps for the infinite crystal [see Fig. 2(a)]. We observe that the frequency range of the stop bands hardly changes with angle of incidence, which is plausible since the stop bands are part of the 3D band gap. This result supports the experimental notion that intense reflectivity peaks collected with an objective with a large numerical aperture give a *bona fide* signature of the 3D band gap [30].

The spectra in Figs. 4(a) and 4(b) reveal Fabry-Pérot fringes at frequencies below the band gap that correspond to standing waves in the finite crystal slab. For p polarization, Fig. 4 reveals an intriguing hybridization of the resonance condition ($R = 0$) of the Fabry-Pérot fringes and of the Brewster angle, which has not yet been observed in experiments. Moreover, reflectivity inside the p-stop band is not affected by the Brewster angle, unlike a 1D Bragg stack as shown in Ref. [52]. In order to characterize this feature, we calculated reflectivity spectra using a higher resolution in frequency and angle of incidence, shown in Fig. 5. We note that the Fabry-Pérot fringes have a constant frequency for angles of incidence up to $\theta = 54^\circ$ before bending. Beyond $\theta = 61^\circ$, the fringes have shifted down in frequency to nearly the frequency of the lower order one at $\theta \leqslant 54^\circ$, e.g., the $n = 2$ fringe at $\tilde{\omega} = 0.24$ ($\theta \leqslant 54^\circ$) shifts to $\tilde{\omega} = 0.15$ ($\theta > 61^\circ$), which is close to the frequency of the $n = 1$ fringe at $\theta \leqslant 54^\circ$. From the effective refractive index ($n_e = 1.68$), we derive the Brewster angle $\theta_B = 59.2^\circ$, which matches the range ($54^\circ \leqslant \theta \leqslant 61^\circ$) of the hybridization. Therefore, we conclude that the hybridization occurs between the Fabry-Pérot resonances and the Brewster angle.

Figure 5 shows that the midpoint of each bend in a fringe increases with increasing frequency and fringe order. We surmise that this shift is the result of an increasing effective index with frequency as a result of increasing band flattening in the approach of a stop gap or band gap, see Fig. 2. We note that at the lowest frequency the midpoint occurs at a smaller angle than θ_B obtained from n_e in the limit $\omega \to 0$. This difference is currently puzzling, since both angles are expected at the same angle at low frequency where no band bending occurs. We speculate that the hybridization probes another effective index than the one derived from the bands at $\omega \to 0$. The radius of curvature of a bend increases while approaching the stop band. A possible cause may be the approach of the 3D photonic band gap that prevents light from entering at a Brewster angle.

For comparison, we have analytically computed the angle- and frequency-resolved reflectivity spectra of a thin film for p polarization (see Appendix B). We find that the Brewster angle is constant with frequency. We also observe that the Fabry-Pérot fringes have a constant frequency at all angles and do not bend near the Brewster angle. These observations on a thin film also pertain to a 1D Bragg stack as shown in Ref. [47]. Therefore, the hybridization between the Fabry-Pérot resonances and the Brewster angle appears to be a characteristic property of the 3D photonic crystal that remains to be observed experimentally.

B. Frequency-resolved reflectivity at normal incidence

We have performed an extensive set of polarization-resolved (s or p) reflectivity calculations at normal incidence to the photonic crystal slab that corresponds to a typical experimental geometry [14,15,22–25,27,30] and since this high-symmetry geometry facilitates data interpretation. Since similar inverse woodpile structures were studied in our group [30], we tuned the parameters to this study, namely a smaller pore radius ($\frac{r}{a} = 0.19$) and a dielectric permittivity $\epsilon = 12.1$, typical for silicon in the near infrared and telecom ranges [30,33]. Figure 6 shows spectra for a thin crystal with a thickness $L = 4c$. Fabry-Pérot fringes are visible for both polarizations in Figs. 6(i) and 6(iii) corresponding to standing waves in the finite crystal. The strong reflectivity peaks near $\tilde{\omega} = 0.45$ indicate stop bands for both s and p polarizations.

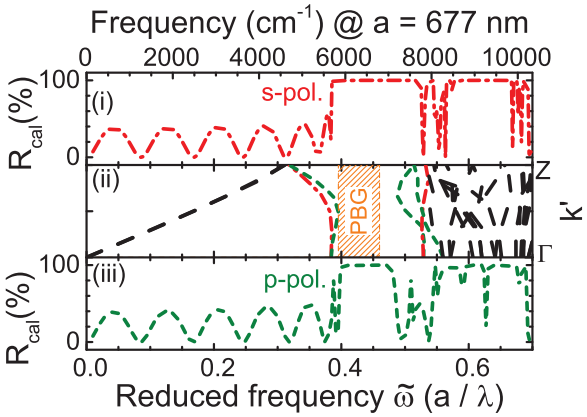

FIG. 6. Calculated reflectivity spectra for a Si inverse woodpile photonic band gap crystal along the ΓZ high symmetry direction in wave vector space. The red curve in (i) and the green curve in (iii) are reflectivity spectra calculated for s and p polarization, respectively. The corresponding band structure for the ΓZ direction is shown in (ii), where the 3D band gap is shown in orange. The wave vector is expressed as $k' = (ka/2\pi)$. The polarization character of bands near the gap is assigned in Fig. 7. The frequency ranges of the s- and p-stop bands agree excellently with corresponding stop gaps in the photonic band structure.

The stop bands at normal incidence appear at a lower frequency than in Fig. 4 since the air fraction is less and hence the average index of the crystal is greater. The p-stop band appears between $\tilde{\omega} = 0.395$ and $\tilde{\omega} = 0.488$ with a broad relative bandwidth 21%. The s-stop band appears between $\tilde{\omega} = 0.385$ and $\tilde{\omega} = 0.526$ and it is about 1.5× broader (relative bandwidth 31%) than the p-stop band. At frequencies beyond $\tilde{\omega} = 0.55$ several bands of high reflectivity appear. In these frequency bands the band structures reveal extremely complex couplings of multiple Bragg conditions [48] that lead to complex band structures that are sometimes also referred to as *spaghetti-like* behavior. Thus these apparent stop bands can be caused by the uncoupled modes of plane waves outside crystals, or by modes whose dispersion relation restricts impedance matching to waves outside the crystal.

The frequency ranges of the s- and the p-stop bands agree very well with corresponding stop gaps in the photonic band structure. Such a comparison allows us to assign the polarization character without need to compute eigenfunctions. Since the third photonic band at the lower stop gap edge (near $\tilde{\omega} = 0.385$) agrees with the lower boundary of the s-stop band, we conclude that this band has dominantly s character. Furthermore, the fourth band is located inside the s-stop band and agrees with the lower edge of the p-stop band at $\tilde{\omega} = 0.395$. Therefore, we conclude that this band must have dominantly p character. Near the upper gap edge, the seventh band near $\tilde{\omega} = 0.526$ agrees with the upper s-stop band edge and is thus likely an s band. The fifth and sixth bands between $\tilde{\omega} = 0.49$ and $\tilde{\omega} = 0.526$ are situated well inside the s-stop band and can therefore only have p character; indeed, these bands lie outside the p-stop band. This assignment of bands 5, 6, and 7 is further supported by the observation that band 7 crosses bands 5 and 6 at $\tilde{\omega} = 0.526$, without revealing avoided crossings.

C. Frequency-resolved reflectivity through a numerical aperture

A recent experimental study by our group reported the signature of a 3D photonic band gap in silicon inverse woodpile crystals [30]. The signature consists of observing overlapping stop bands for a large solid angle of $(1.76 \pm 0.18)\pi$. The experiments were performed on crystals with an extent of $L^3 = 12^3$ unit cells on top of bulk silicon. Polarization-resolved reflectivity spectra were measured using a reflecting objective with NA = 0.65 and Obscuration = 13.3%. Thus, the incident light has an angular spread from about 6° to 40° off normal. To accurately mimic the NA of a microscopic objective in an experiment, calculations should be performed for all wave vectors within the solid angle of the conical incident beam. Moreover, one should calculate fields and add these coherently to mimic the focusing by the objective, before taking the absolute square to obtain the intensity as in the experiments [30]. Since this procedure is currently prohibitively computer expensive, we approximate this angular spread of the incident and collected light without an attempt to average. We calculated reflectivity spectra for angles of incidence from 6° to 40° off normal in the YZ plane for each polarization, see Fig. 8. We observe strong angle-dependent reflectivity variations near the lower and the upper edges of the stop band. The intense angle-independent reflectivity peaks near $\tilde{\omega} = 0.45$ indicate the stop bands for both s and p polarizations. A comparison between the angle-independent high reflectivity ranges (Fig. 8) and the angle-resolved reflectivity spectra centered at 0° (Fig. 7) shows that there are shifts and changes in stop bandwidths. For s polarization, the stop band edge at half height shifts from $\tilde{\omega} = 0.385$ to 0.383 (lower edge) and from $\tilde{\omega} = 0.526$ to 0.48 (upper edge), hence the stop band center shifts down from $\tilde{\omega} = 0.455$ to 0.432, and the width narrows from $\Delta\tilde{\omega} = 0.141$ to 0.097.

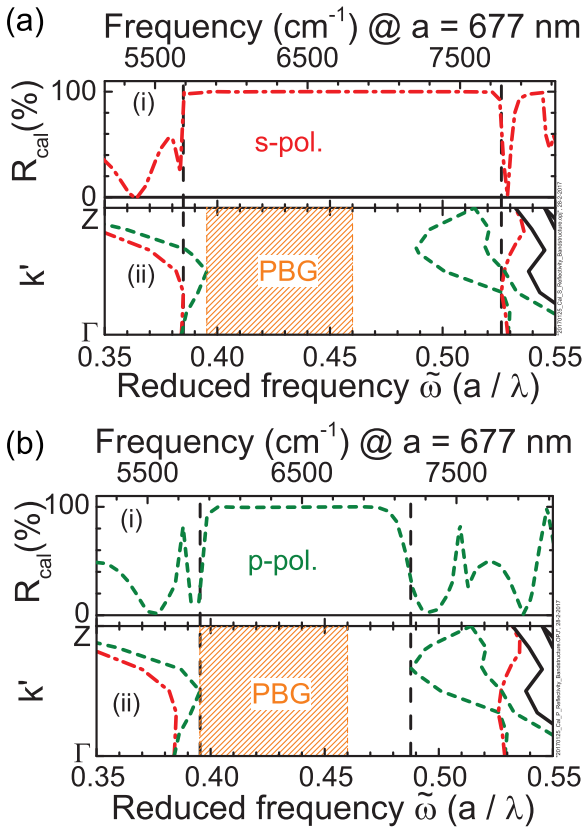

FIG. 7. Reflectivity near the stop band for (a) s- and (b) p-polarized light for Si inverse woodpile crystals. In (i), red dashed-dotted and green dashed curves are calculated results, as in Fig. 6. (ii) The band structures for (a) s- and (b) p-polarized light, where the 3D band gap is shown in orange. The wave vector is expressed as $k' = (ka/2\pi)$. The vertical black dashed lines indicate the edges of the stop band (i) and the matching stop gap edges (ii). Near the stop gap edges, we identify s bands (red dashed-dotted curves) and p bands (green dashed curves).

We now compare the measured spectra for the stop bands in the ΓX and the ΓZ directions with the angle-independent calculated intense reflectivity peak, as shown in Fig. 8. In particular, we discuss the central frequency, the bandwidth, and the maximum reflectivity. In the ΓX and the ΓZ directions, the central frequencies for s polarization and p polarization in the calculation and in the experiment agree well to nearly within both error bars [49]. From the Bragg diffraction condition [19], the central frequency ω_c in terms of the effective index is

$$\omega_c = \frac{1}{n_e}\frac{m\pi c}{L}, \tag{1}$$

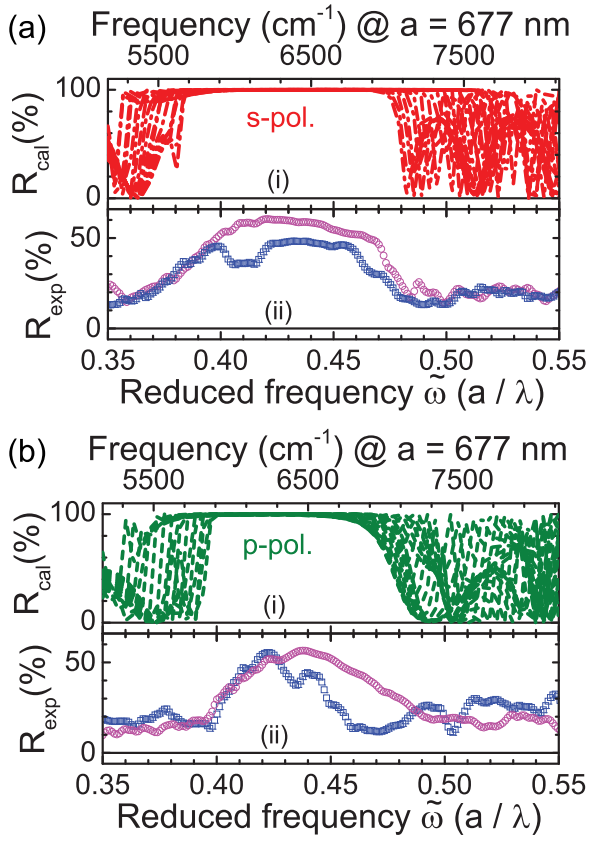

FIG. 8. Comparison between numerical calculations and experimental results for the reflectivity peaks near the stop band for (a) s- and (b) p-polarized light for Si inverse woodpile crystals. (i) The calculated results, where red dashed-dotted and green dashed curves are reflectivity spectra for angles of incidence from 6° to 40° off normal in the ΓZ direction as well as in the equivalent ΓX direction. In (ii), blue squares are measurements from Ref. [30] in the ΓZ direction, and magenta circles in the equivalent ΓX direction. The top ordinate shows the frequency in wave numbers (cm^{-1}) for a lattice parameter $a = 677$ nm as in the experiments.

with m the integer diffraction order. From the good agreement of the central frequencies, we deduce from Eq. (1) that n_e in the calculations ($n_e = 2.28$) is close to the one in the experiments. Therefore, we conclude that the total volume fraction of the high-index material (Si) in the calculations matches with the experimental one.

Figure 8(a) shows that for s polarization, the bandwidths in the calculation and in the experiment in the ΓX direction agree well to nearly within both error bars. The comparison of the bandwidths in the calculation and in the experiment in the ΓZ direction exhibits a small difference for s polarization, which is outside the specified error bars [50]. Figure 8(b) shows that for p polarization, in the ΓX direction the calculated bandwidth agrees well to the measured bandwidth to nearly within both error bars. In the ΓZ direction, the comparison of bandwidths in the calculation and in the experiment exhibits a small difference for p polarization, outside the specified error bars [51]. Therefore, the calculated bandwidth and the measured bandwidth agree in ΓX direction, but disagree in ΓZ direction for both polarizations. The experimental results in Fig. 8 show that the bandwidth for the ΓZ direction is smaller than the bandwidth for the ΓX direction. The bandwidth for 3D silicon inverse woodpile photonic crystals increases with increasing pore radius to a maximum at pore radius $\frac{r}{a} = 0.245$ in the gap map in Ref. [30]. Therefore, the bandwidth for the ΓZ direction can be smaller than the bandwidth for the ΓX direction if the pore radius in the ΓZ direction is smaller than the one in the ΓX direction for these crystals. The fabrication process could result in different pore radii $\frac{r}{a}$ in the ΓZ and the ΓX directions. We surmise that the $\frac{r_{\Gamma Z}}{a}$ ratio is smaller than $\frac{r}{a} = 0.19$, whereas the $\frac{r_{\Gamma X}}{a}$ ratio is larger than $\frac{r}{a} = 0.19$, but smaller than optimal optimal pore size $\frac{r}{a} = 0.245$ [30]. Simultaneously, the total volume fraction is apparently constant in view of the central frequencies above. Therefore, we hypothesize that the difference in measured reflectivity spectra for two symmetry-related directions ΓX and ΓZ is due to the fabrication process resulting in different pore radii for these directions. Hence, our calculations reveal that an angle-independent strong reflectivity spectrum over an angular spread of the incident light for a certain experiment provides an improved interpretation of the reflectivity measurements and an insight in the crystal structure.

Figure 8 shows marked differences between the maximum reflectivity in calculations and in experiments. In the experimental work, the limited maximum reflectivity (67%) was attributed to the finite thickness of the crystal, to angle of incidence, and to surface roughness, although no theoretical or numerical support was offered for these notions. In reflectivity spectra shown in Figs. 6 and 9 (explained below in Sec. III D), we observe strong reflectivity peaks even for thin crystals. This implies that the finite size is not a critical limiting factor for reflectivity. Figures 4(a) and 4(b) show that the observed stop bands hardly change with angle of incidence. This observation supports the experimental assertion that intense reflectivity peaks measured with an objective with a large numerical aperture provide a faithful signature of the 3D photonic band

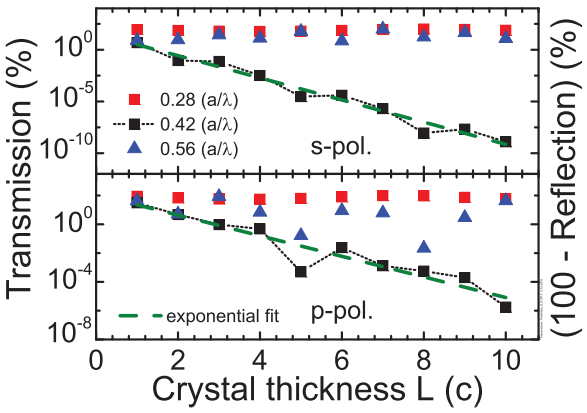

FIG. 9. Transmission versus thickness for a silicon inverse woodpile photonic crystal in the ΓZ direction for s (top) and p polarizations (bottom). Red squares, black circles, and blue triangles pertain to frequencies below, inside, and above the stop gap, respectively. The green dashed lines are the exponential decay of transmission with crystal thickness at frequencies in the stop gap [Eq. (2)]. The black dashed line is a guide to the eye that shows modulations in the stop band.

gap. Extensive numerical studies are called for in order to ascertain the impact of roughness of the crystal-air interface, as well as roughness inside the pores.

D. Finite-size effects: Bragg attenuation length

To investigate the effect of finite thickness of the crystal, we calculated the transmission for thicknesses between $L = 1c$ and $10c$. Figure 9 shows that for a given frequency inside the stop gap, the transmission decays exponentially for both s and p polarizations. For frequencies below or above the stop gap, the transmission is nearly constant, with some small variations with crystal thickness as a result of the Fabry-Pérot fringes that vary with crystal thickness, as is well known for 1D Bragg stacks [52,53].

Inside a stop gap the complex wave vector k has a nonzero imaginary component $\mathrm{Im}(k)$ since the waves are damped by Bragg diffraction interference [24,52,54]. Thus, we write the transmission T in a stop band as [55–57]

$$T(\omega, L) = \exp\left(-\frac{L}{L_B(\omega)}\right), \tag{2}$$

with L_B the Bragg attenuation length equal to

$$L_B(\omega) = \frac{1}{\mathrm{Im}(k)(\omega)} \tag{3}$$

that gives the distance covered by incident light until it has exponentially decayed to a fraction $1/e$. Figure 9 reveals that even inside the stop band the transmission shows modulations, as was previously identified in 1D stacks [52,53]. The reason is that transmission also contains the effects of both front and back crystal surfaces.

The Bragg attenuation length is usually expressed in terms of the distance between lattice planes d_{hkl}. Therefore, we reduce the Bragg length to the $\{hkl = 220\}$ lattice spacing d_{220} that equals $d_{220} = c/2$. The s-polarized data in Fig. 9 agree well with Eq. (2) with a slope that yields a Bragg attenuation length $L_B = 0.74 d_{220}$. For the p-polarized data in Fig. 9, we obtain a Bragg attenuation length $L_B = 1.21 d_{220}$ at the gap center, which is about $1.5\times$ larger than for s polarization at the gap center. This observation agrees quantitatively with the reflectivity spectrum where the s-polarized stop band is also $1.5\times$ broader than the p-polarized stop band (see Fig. 6). This behavior can be understood as follows: The Bragg attenuation length at the center frequency of a stop gap of a Bragg stack satisfies [13]

$$L_B = \frac{2d}{\pi S} \simeq \frac{2d}{\pi}\frac{\omega_c}{\Delta\omega}. \tag{4}$$

The photonic interaction strength S is defined as the polarizability per volume of a unit cell [58,59] and is estimated from the relative frequency bandwidth of the stop band for a dominant reciprocal lattice vector as $S \approx \frac{\Delta\omega}{\omega_c}$ [13]. We find that the Bragg lengths are shorter by a factor 6 to 9 than the earlier experimental estimate in Ref. [30] that was derived from the width of the stop bands. Hence, crystals with a thickness of 12 unit cells studied in these experiments are effectively in the thick crystal limit since $\frac{L}{L_B} = 5$ to 8. Regarding the reason why the Bragg length obtained from the stop bandwidth [Eq. (4)] differs from the Bragg length determined from the thickness-dependent transmission [Eq. (2)], we speculate that Eq. (4) pertains to a simple stop gap typical of a Bragg stack with only one band below and one band above the gap whose Bloch-state repulsion yields a gap at wave vectors equal to the Brillouin zone boundary [19], in notable absence of multiple Bragg diffraction [60]. In contrast, Figs. 7(a) and 7(b) show that the dominant stop gap is bounded by multiple Bragg behavior, as is apparent from the pertinent elevated Miller indices (see Sec. IV A), and since the gap is bounded by bands at wave vectors inside the Brillouin zone (not the zone boundary). Since multiple Bragg diffraction is known to lead to frequency and wave vector shifts of gaps, as well as changes of gap widths, it is quite conceivable that in this situation Eq. (4) is not equivalent anymore to Eq. (2).

IV. DISCUSSION

A. Role of geometrical structure factor

The polarization-resolved reflectivity spectra for the cubic diamondlike inverse woodpile structure in Fig. 6 reveal Fabry-Pérot fringes that correspond to standing waves in the periodically layered finite crystal. There are three corollaries based on theory for a periodic layered Bragg reflector with a thickness of N unit cells [52]. First, a reflectivity peak occurs at the center of the stop gap. Second, between any two stop gaps there are exactly $(N-1)$ troughs in the reflectivity spectra. Third, there are exactly $(N-2)$ side lobes to the reflectivity peak.

The band structure in Fig. 6(ii) shows two stop gaps in the ΓZ direction. A narrow stop gap appears near $\tilde{\omega} = 0.311$ and the broad stop gap appears near $\tilde{\omega} = 0.39$. We now interpret the spectra in Figs. 6(i) and 6(iii) for $N = 4$ unit cells in terms of the three corollaries above. For s-polarization reflectivity in Fig. 6(i), we observe a peak near $\tilde{\omega} = 0.45$, at the center of the second stop gap. Surprisingly, there is no peak near the center of the first stop gap at variance with the first corollary. This spectrum reveals four troughs between zero frequency and the first stop gap, the fifth trough near the center of the first stop gap, and two troughs between the first and second order stop gap; which seems mutually inconsistent and at variance with the second corollary. For p-polarized reflectivity in Fig. 6(iii), we observe a reflectivity peak near the $\tilde{\omega} = 0.45$, which corresponds to the center of the second stop gap. Also, no reflectivity peak appears near the center of the first stop gap, at variance with the first corollary. In this spectrum, there are four troughs between zero frequency and the first stop gap, and three troughs between the first and second order stop gap; which seems mutually inconsistent and at variance with the second corollary. Therefore, the above observations for p polarization do not agree with the observations for s polarization.

To remedy this seeming disagreement, we consider the geometrical structure factor $S_{\mathbf{K}}$ that indicates the degree to which interference of waves scattered from identical ions within the crystal basis inside the unit cell affect the intensity of a Bragg peak associated with reciprocal lattice vector $\mathbf{K}$ [19]. Since the intensity of the Bragg peak is proportional to the square of the absolute value of $S_{\mathbf{K}}$, the Bragg peak vanishes when $S_{\mathbf{K}}$ vanishes. For a conventional cubic unit cell of the monatomic diamond structure, $S_{\mathbf{K}} = 0$ if the sum of Miller

indices equals twice an odd number n: $h+k+l=2n$. In Fig. 6 the stop gap near $\tilde{\omega}=0.31$ in ΓZ direction corresponds to a first-order stop gap for $\{hkl=110\}$ lattice planes in the conventional diamond structure [19]. Since the sum of Miller indices in {110} is twice the odd number 1, the first-order stop gap in the cubic inverse woodpile photonic structure has zero geometrical structure factor ($S_{\mathbf{K}}=0$) and hence zero associated Bragg reflection. If the sum of Miller indices $(h+k+l)$ is twice an even number, $S_{\mathbf{K}}$ is maximum and equals $S_{\mathbf{K}}=2$. The stop gap near $\tilde{\omega}=0.4$ in Fig. 6 is a second-order stop gap for $\{hkl=110\}$ and corresponds to $\{hkl=220\}$ defined using x-ray diffraction in a conventional cubic diamond structure [19]. Since the sum of Miller indices in {220} equals twice an even number, the second-order stop gap has $S_{\mathbf{K}}\neq 0$. Therefore, the second-order stop gap has a maximal structure factor. Hence, only the second-order stop gap in a cubic diamondlike inverse woodpile structure reveals appreciable Bragg reflection and should therefore be considered for the analysis of the observed Fabry-Pérot fringes in the reflectivity spectra.

The distance between lattice planes equals $d_{220}=c/2$ for the dominant second-order stop gap with Miller indices $\{hkl=220\}$. Therefore, the $L=4c$ crystal thickness used in the computational cell in Fig. 6 corresponds to a thickness $L=Nd_{220}=8d_{220}$ in terms of a periodic layered medium (a Bragg stack) [52]. In Fig. 6 we observe reflectivity peaks near $\tilde{\omega}=0.45$ for s and p polarizations, which are at the center of the s and p stop gaps. This satisfies the first corollary for the periodic layered medium. Second, there are exactly $(N-1)=7$ troughs in the reflectivity spectra between zero frequency and the main stop gap corresponding to $N=8$ lattice planes in the crystal, in agreement with the second corollary above. Third, there are $(N-2)=6$ side lobes in the reflectivity spectra, again agreeing with $N=8$ lattice planes by the third corollary. These three corollaries confirm that the number of Fabry-Pérot fringes in our reflectivity spectra agrees with the theory for a Bragg reflector [52]. Moreover, this episode reminds us that it is the number of lattice planes that is fundamental in the thickness of a finite crystal, rather than the number of unit cells.

B. Comparison to other inverse woodpiles and woodpiles

The silicon inverse woodpile photonic crystal studied in Ref. [26] has a 3D structure consisting of two interpenetrating hexagonal pore sets that corresponds to an orthorhombic symmetry. Therefore, the first Brillouin zone is distorted compared to the Brillouin zone of an fcc lattice. This study reported reflectivity spectra in one high-symmetry direction using unpolarized light. The strong reflectivity peak denotes the stop band along the z direction. The stop band is shown to agree with the stop gap obtained from the band structure. Since the crystal has orthorhombic symmetry, the ΓX stop gap is not symmetry related in k space to the ΓZ stop gap. Therefore, the stop band is representative for a limited range of solid angles. The limited reflectivity was attributed to the numerical aperture, to surface roughness, and to roughness at the pore walls.

The silicon woodpile photonic crystals studied in Ref. [27] has lattice parameters in a ratio $\frac{c}{a}=1.15$, hence the crystals are not cubic but tetragonal. This study reports reflectivity spectra in one high symmetry direction. To mimic the angular spread of the incident light in the experiments, reflectivity spectra were calculated for many incident angles in the relevant range and averaged over the obtained results. It is unknown whether this average includes the coherent field addition and the NA filling that is needed to compare to experiments (see Sec. III C). A qualitative agreement between the stop band observed in experiment, the stop band identified from calculation, and the stop gap calculated from the band structure is found. The maximum observed reflectivity is accredited to measurement limitations, to unspecified deviations from perfect periodicity, and to surface roughness. Since the crystal is not cubic, the ΓX stop gap is not symmetry related to the ΓZ stop gap. Therefore, the stop band is representative for a limited range of solid angles. The polarization of the light used in the calculation of reflectivity spectra is unspecified, so polarization character cannot be attributed to the bands by comparing reflectivity spectra with the band structure. Nevertheless, the calculated reflectivity spectra reveal Fabry-Pérot fringes at wavelengths above the stop band that correspond to standing waves in the finite-sized crystal, as also seen in Fig. 4. The number of unit cells in the structure is unspecified, so it is not feasible to verify the theory for a periodic layered Bragg reflector for the number of Fabry-Pérot fringes. The calculations were reported for a fixed crystal thickness, so the Bragg attenuation length was not deduced. Since the calculated reflectivity spectra are angle averaged, a possible Brewster angle is not visible. Our calculations have shown that the finite size deviation from the perfect periodicity is not responsible for the limited maximum reflectivity. Thus, we conclude that the the maximum observed reflectivity is likely limited by the invoked measurement limitations and surface roughness.

C. Back reflector for solar cells

The efficiency of silicon photovoltaic cells critically depends on efficient ways to trap and absorb light [61,62]. It remains a challenge to have thin film c-Si solar cells trap a significant part of solar energy [7]. Increasing wafer thickness results in longer diffusion lengths, but increases costs. Traditionally, light trapping in solar cells rest on controlling light ray paths using geometrical optics, e.g., by scattering incident light via surface texturing and back reflection into the solar cells via a reflector. In practice, perfect scattering and reflection are difficult to obtain, which limits the attainable efficiency and power generation of solar cells. Recently, it has been shown that the light trapping approaches based on wave optics outperform all geometrical optics approaches for a certain range of frequencies [20]. One can employ specially nanodesigned structures, such as 3D photonic crystals, notably those with a complete 3D photonic band gap.

The results in Fig. 9 reveal that a reflectivity in excess of $R>99\%$ (hence $T<1\%$) is found inside the stop band already for thin 3D silicon photonic band gap crystals, with a thickness as small as $L\geqslant 2c$ for s polarization, and $L\geqslant 3c$ for p polarization. In addition, by combining Figs. 4(a) and 4(b), we note that an angle- and polarization-independent range of high reflectivity appears between $\tilde{\omega}=0.4962$ and $\tilde{\omega}=0.6379$ with a broad 25% relative bandwidth, much more

than is predicted for (even thicker) 1D Bragg stacks [52]. Hence, our calculations support the assertion that a 3D silicon photonic crystal could serve as an efficient back reflector in a solar cell in order to enhance the efficiency.

V. CONCLUSIONS

We have studied by numerical simulation the reflectivity of 3D photonic crystals with a 3D complete photonic band gap, to interpret recent experiments. We employed the finite element method to study crystals with the cubic diamondlike inverse woodpile structure, with a dielectric function similar to silicon. The crystals are surrounded by vacuum, and thus have a finite support as in the experiments. We observe that the stop band hardly changes with incident angle, which supports the experimental notion that strong reflectivity peaks measured with large numerical aperture gives a faithful signature of the 3D band gap. We observe an intriguing hybridization of the Fabry-Pérot resonances and the Brewster angle in our calculations, which seems a characteristic property of 3D photonic band gap crystals. From the intense reflectivity peaks, we infer that the maximum reflectivity observed in the experiments is not limited by finite size of the crystal. Our calculated polarization-resolved reflectivity spectra show that the frequency ranges of the s and p stop bands agree well with the corresponding stop gaps in the photonic band structure. From the comparison we assign bands in the band structure near these stop bands to have dominantly s or p character. The comparison between angle-independent numerical calculations and experimental results provides an improved interpretation of the reflectivity measurements and a new insight in the crystal structure (unequal pore sizes in different directions). We find that the Bragg attenuation lengths in the stop bands are smaller than the earlier estimates based on the width of the stop band by a factor of 6 to 9. Our results indicate that 3D silicon photonic band gap crystals merit study as possible candidates for back reflectors in a solar cell in order to enhance the photovoltaic efficiency.

ACKNOWLEDGMENTS

It is a pleasure to thank Olindo Isabella, Ad Lagendijk, Allard Mosk, Oluwafemi Ojambati, Ravitej Uppu, and Rebecca Saive. W.L.V. thanks Ho-Kwang Mao, Larry Finger, and Russell Hemley for teaching him in 1990 of the crystal structure factor and its role in forbidden Bragg peaks of diamond, notably in diamond cells at very high megabar pressures. Deva thanks Pepijn Pinkse for his idea of approximating the NA of a microscopic objective. This research is supported by the Shell-NWO/FOM programme "Computational Sciences for Energy Research" (CSER), by the FOM programme "Stirring of light!," as well as by NWO, STW, and the MESA+ Institute for Nanotechnology (Applied Nanophotonics, ANP).

APPENDIX A: ANALYTICAL VALIDATION OF THE NUMERICAL SCHEME WITH A SEMI-INFINITE HOMOGENEOUS MEDIUM

To validate our numerical scheme, we calculate reflectivity spectra of a system that can be analytically analyzed using Fresnel's equations, namely a homogeneous dielectric medium [63]. We consider p-polarized plane waves at a single frequency with a range of angles of incidence. We replace the photonic crystal and the air layer on the right in Fig. 3(a) with a medium with dielectric permittivity $\epsilon = 12.1$. This results in a semi-infinite homogeneous medium that is separated from the source by an air layer. The finite element mesh used in the numerical calculation consists of 18 732 tetrahedra per crystal unit cell (unit cell defined in terms of the lattice parameter c), somewhat less than the number of tetrahedra in the finite element mesh used for the 3D photonic crystal. The angular resolution is 2°.

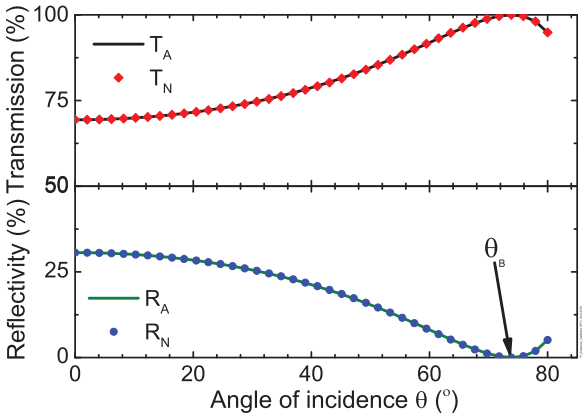

FIG. 10. Analytical calculation versus numerical computation for reflection and transmission spectra of semi-infinite dielectric medium for p polarization. The medium has dielectric permittivity $\epsilon = 12.1$. The analytically calculated reflectivity (R_A) and transmission (T_A) are shown in green and black lines, respectively. Blue circles and red diamonds represent the numerically computed reflectivity (R_N) and transmission (T_N), respectively. θ_B denotes the Brewster angle.

In Fig. 10 we show the calculated reflectivity and transmission spectra of a semi-infinite homogeneous medium for the above defined computational cell. We note that the numerical calculation agrees very well with the analytical calculation. We observe the Brewster angle at $\theta_B = 74°$, which matches the value obtained from an analytical calculation [63]. To calculate the relative error δT_{rel} between the numerical calculation and

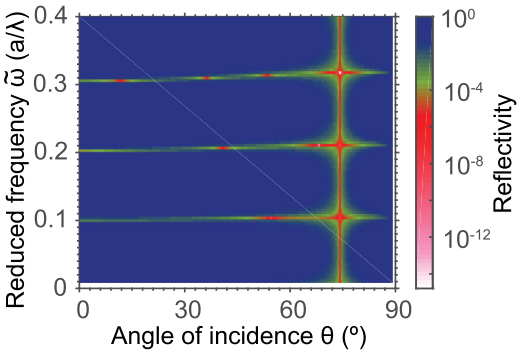

FIG. 11. Analytically calculated angle- and frequency-resolved reflectivity spectra of a thin dielectric film for p polarization. The film has a dielectric permittivity $\epsilon = 12.1$. The Brewster angle at $\theta_B = 73°$ is constant with frequency.

the analytical result, we employ the definition

$$\delta T_{\rm rel} \equiv \frac{1}{n}\sqrt{\left[\sum_{i=1}^{n}\left(\frac{(T_{A,i}-T_{N,i})^2}{T_{A,i}^2}+\frac{(R_{A,i}-R_{N,i})^2}{R_{A,i}^2}\right)\right]}, \tag{A1}$$

with $(T_{N,i}, R_{N,i})$ the numerical transmission and reflectivity, and $(T_{A,i}, R_{A,i})$ the analytical transmission and reflectivity. For the solution shown in Fig. 10, the error is only about $\delta T_{\rm rel} = 6\times10^{-4}$, hence we consider the calculation to be converged.

APPENDIX B: BREWSTER ANGLE FOR A THIN FILM

To find the dependence of the Brewster angle on frequency, we have analytically calculated the angle-resolved and frequency-resolved spectra for a thin film [64]. We consider p-polarized incident waves for angles of incidence up to 89° off the normal. Figure 11 shows Fabry-Pérot fringes corresponding to the standing waves in the thin dielectric film. We note that the Fabry-Pérot fringes have a nearly constant frequency for all angles of incidence. We observe a Brewster angle at $\theta_B = 73°$ that is independent of frequency, as expected for a dispersionless film.

[1] V. P. Bykov, Spontaneous emission in a periodic structure, Sov. Phys. JETP **35**, 269 (1972).

[2] E. Yablonovitch, Inhibited Spontaneous Emission in Solid-State Physics and Electronics, Phys. Rev. Lett. **58**, 2059 (1987).

[3] S. John, Strong Localization of Photons in Certain Disordered Dielectric Superlattices, Phys. Rev. Lett. **58**, 2486 (1987).

[4] J. D. Joannopoulos, P. R. Villeneuve, and S. Fan, Photonic crystals: Putting a new twist on light, Nature (London) **386**, 143 (1997).

[5] C. Lopez, Materials aspect of photonic crystals, Adv. Mater. **15**, 1679 (2003).

[6] J. M. Lourtioz, H. Benisty, V. Berger, J.-M. Gérard, D. Maystre, and A. Tchelnokov, *Photonic Crystals: Towards Nanoscale Photonic Devices* (Springer, Heidelberg, 2005).

[7] J. D. Joannopoulos, S. G. Johnson, J. N. Winn, and R. D. Meade, *Photonic Crystals: Molding the Flow of Light* (Princeton University Press, Princeton NJ, 2008).

[8] Edited by M. Ghulinyan and L. Pavesi, *Light Localisation and Lasing: Random and Pseudorandom Photonic Structures* (Cambridge University Press, Cambridge, 2015).

[9] A. F. Koenderink, L. Bechger, H. P. Schriemer, A. Lagendijk, and W. L. Vos, Broadband Fivefold Reduction of Vacuum Fluctuations Probed by Dyes in Photonic Crystals, Phys. Rev. Lett. **88**, 143903 (2002).

[10] S. Ogawa, M. Imada, S. Yoshimoto, M. Okano, and S. Noda, Control of light emission by 3D photonic crystals, Science **305**, 227 (2004).

[11] P. Lodahl, A. F. van Driel, I. S. Nikolaev, A. Irman, K. Overgaag, D. Vanmaekelbergh, and W. L. Vos, Controlling the dynamics of spontaneous emission from quantum dots by photonic crystals, Nature (London) **430**, 654 (2004).

[12] M. D. Leistikow, A. P. Mosk, E. Yeganegi, S. R. Huisman, A. Lagendijk, and W. L. Vos, Inhibited Spontaneous Emission of Quantum Dots Observed in a 3D Photonic Band Gap, Phys. Rev. Lett. **107**, 193903 (2011).

[13] W. L. Vos and L. A. Woldering, in Ref. [8], Chap. 8, pp. 180–214, also available from http://arxiv.org/abs/1504.06803.

[14] J. G. Fleming, S.-Y. Lin, I. El-Kady, R. Biswas, and K. M. Ho, All-metallic three-dimensional photonic crystals with a large infrared bandgap, Nature (London) **417**, 52 (2002).

[15] S. E. Han, A. Stein, and D. J. Norris, Tailoring Self-Assembled Metallic Photonic Crystals for Modified Thermal Emission, Phys. Rev. Lett. **99**, 053906 (2007).

[16] A. Tandaechanurat, S. Ishida, D. Guimard, M. Nomura, S. Iwamoto, and Y. Arakawa, Lasing oscillation in a three-dimensional photonic crystal nanocavity with a complete bandgap, Nat. Photon. **5**, 91 (2011).

[17] D. Zhou and R. Biswas, Photonic crystal enhanced light-trapping in thin film solar cells, J. Appl. Phys. **103**, 093102 (2008).

[18] T. Ergin, N. Stenger, P. Brenner, J. B. Pendry, and M. Wegener, Three-dimensional invisibility cloak at optical wavelengths, Science **328**, 337 (2010).

[19] N. W. Ashcroft and N. D. Mermin, *Solid State Physics* (Holt, Rinehart and Winston, New York, 1976).

[20] P. Bermel, C. Luo, L. Zeng, L. C. Kimerling, and J. D. Joannopoulos, Improving thin-film crystalline silicon solar cell efficiencies with photonic crystals, Opt. Express **15**, 16986 (2007).

[21] J. G. Fleming and S.-Y. Lin, Three-dimensional photonic crystal with a stop band from 1.35 to 1.95 μm, Opt. Lett. **24**, 49 (1999).

[22] A. Blanco, E. Chomski, S. Grabtchak, M. Ibisate, S. John, S. W. Leonard, C. Lopez, F. Meseguer, H. Miguez, J. P. Mondia, G. A. Ozin, O. Toader, and H. M. van Driel, Large-scale synthesis of a silicon photonic crystal with a complete three-dimensional bandgap near 1.5 micrometres, Nature (London) **405**, 437 (2000).

[23] S. Noda, K. Tomoda, N. Yamamoto, and A. Chutinan, Full three-dimensional photonic bandgap crystals at near-infrared wavelengths, Science **289**, 604 (2000).

[24] Y. A. Vlasov, X. Bo, J. C. Sturm, and D. J. Norris, On-chip natural assembly of silicon photonic bandgap crystals, Nature (London) **414**, 289 (2000).

[25] G. Subramania and S.-Y. Lin, Fabrication of three-dimensional photonic crystal with alignment based on electron beam lithography, Appl. Phys. Lett. **85**, 5037 (2004).

[26] J. Schilling, J. White, A. Scherer, G. Stupian, R. Hillebrand, and U. Gösele, Three-dimensional macroporous silicon photonic crystal with large photonic band gap, Appl. Phys. Lett. **86**, 011101 (2005).

[27] I. Staude, M. Thiel, S. Essig, C. Wolff, K. Busch, G. Von Freymann, and M. Wegener, Fabrication and characterization of silicon woodpile photonic crystals with a complete bandgap at telecom wavelengths, Opt. Lett. **35**, 1094 (2010).

[28] W. M. Robertson, G. Arjavalingam, R. D. Meade, K. D. Brommer, A. M. Rappe, and J. D. Joannopoulos, Measurement of Photonic Band Structure in a Two-Dimensional Periodic Dielectric Array, Phys. Rev. Lett. **68**, 2023 (1992).

[29] K. Sakoda, Symmetry, degeneracy, and uncoupled modes in two-dimensional photonic lattices, Phys. Rev. B **52**, 7982 (1995).

[30] S. R. Huisman, R. V. Nair, L. A. Woldering, M. D. Leistikow, A. P. Mosk, and W. L. Vos, Signature of a three-dimensional photonic band gap observed with silicon inverse woodpile photonic crystals, Phys. Rev. B **83**, 205313 (2011).

[31] K. M. Ho, C. T. Chan, C. M. Soukoulis, R. Biswas, and M. Sigalas, Photonic band gaps in three dimensions: New layer-by-layer periodic structures, Solid State Commun. **89**, 413 (1994).

[32] R. Hillebrand, S. Senz, W. Hergert, and U. Gösele, Macroporous-silicon-based three-dimensional photonic crystal with a large complete band gap, J. Appl. Phys. **94**, 2758 (2003).

[33] L. A. Woldering, A. P. Mosk, R. W. Tjerkstra, and W. L. Vos, The influence of fabrication deviations on the photonic band gap of three-dimensional inverse woodpile nanostructures, J. Appl. Phys. **105**, 093108 (2009).

[34] F. García-Santamaría, M. Xu, V. Lousse, S. Fan, P. V. Braun, and J. A. Lewis, A germanium inverse woodpile structure with a large photonic band gap, Adv. Mater. **19**, 1567 (2007).

[35] A. Hermatschweiler, A. Ledermann, G. A. Ozin, M. Wegener, and G. von Freymann, Fabrication of silicon inverse woodpile photonic crystals, Adv. Funct. Mater. **17**, 2273 (2007).

[36] B. Jia, S. Wu, J. Li, and M. Gu, Near-infrared high refractive-index three-dimensional inverse woodpile photonic crystals generated by a sol-gel process, J. Appl. Phys. **102**, 096102 (2007).

[37] T. Tajiri, S. Takahashi, Y. Ota, J. Tatebayashi, S. Iwamoto, and Y. Arakawa, Demonstration of a three-dimensional photonic crystal nanocavity in a ⟨110⟩-layered diamond structure, Appl. Phys. Lett. **107**, 071102 (2015).

[38] L. A. Woldering, R. W. Tjerkstra, H. V. Jansen, I. D. Setija, and W. L. Vos, Periodic arrays of deep nanopores made in silicon with reactive ion etching and deep UV lithography, Nanotechnology **19**, 145304 (2008).

[39] J. M. van den Broek, L. A. Woldering, R. W. Tjerkstra, F. B. Segerink, I. D. Setija, and W. L. Vos, Inverse-woodpile photonic band gap crystals with a cubic diamond-like structure made from single-crystalline silicon, Adv. Funct. Mater. **22**, 25 (2012).

[40] D. A. Grishina, C. A. M. Harteveld, L. A. Woldering, and W. L. Vos, Method to make a single-step etch mask for 3D monolithic nanostructure, Nanotechnology **26**, 505302 (2015).

[41] H. H. Li, Refractive index of silicon and germanium and its wavelength and temperature derivatives, J. Phys. Chem. Ref. Data **9**, 561 (1993).

[42] From scanning electron microscopy the lattice parameter was found to be $a = 693 \pm 10$ plus the error margin of the SEM that amounts to 2% to 3% [39]. Therefore, we take $a =$ 677 nm, which shows the best match of the central frequencies in the calculations and in the experiments, see Fig. 8. Moreover, for $a = 677$ nm, experimental stop bands agree best with the calculated photonic band gap, see Fig. 8.

[43] S. G. Johnson and J. D. Joannopoulos, Block-iterative frequency-domain methods for Maxwell's equations in a planewave basis, Opt. Express **8**, 173 (2001).

[44] Throughout this paper, we express frequency as a reduced frequency $\tilde{\omega} = \omega a/(2\pi c')$, with ω the frequency, a the lattice parameter, and c' the speed of light that is not to be confused with the lattice parameter c. In this definition, the reduced frequency $\tilde{\omega}$ is expressed in units of (a/λ).

[45] COMSOL Multiphysics® v. 5.2. www.comsol.com, COMSOL AB, Stockholm, Sweden.

[46] J. M. Jin, *The Finite Element Method in Electromagnetics* (Wiley-IEEE, New York, 2000).

[47] Y. Shen, D. Ye, I. Celanovic, S. G. Johnson, J. D. Joannopoulos, and M. Solijačić, Optical broadband angular selectivity, Science **343**, 1499 (2014).

[48] W. L. Vos and H. M. van Driel, Higher order Bragg diffraction by strongly photonic fcc crystals: Onset of a photonic bandgap, Phys. Lett. A **272**, 101 (2000).

[49] For s polarization, the calculated central frequency is $6374 \pm 25\,\mathrm{cm}^{-1}$, while the measured central frequency was reported to be $6355 \pm 32\,\mathrm{cm}^{-1}$ in the ΓX direction and $6288 \pm 32\,\mathrm{cm}^{-1}$ in the ΓZ direction. For p polarization, the calculated central frequency is $6436 \pm 51\,\mathrm{cm}^{-1}$, while the measured central frequency was reported to be $6500 \pm 32\,\mathrm{cm}^{-1}$ in the ΓX direction and $6285 \pm 32\,\mathrm{cm}^{-1}$ in the ΓZ direction.

[50] For s polarization, the calculated bandwidth is $1433 \pm 25\,\mathrm{cm}^{-1}$ (namely from 5657 to 7090 cm^{-1}), while the measured bandwidth was reported to be $1410 \pm 32\,\mathrm{cm}^{-1}$ (namely from 5650 to 7060 cm^{-1}) in the ΓX direction and $1325 \pm 32\,\mathrm{cm}^{-1}$ (namely from 5625 to 6950 cm^{-1}) in the ΓZ direction.

[51] For p polarization, the calculated bandwidth is $1190 \pm 51\,\mathrm{cm}^{-1}$ (namely from 5841 to 7031 cm^{-1}), while the measured bandwidth was reported to be $1150 \pm 32\,\mathrm{cm}^{-1}$ (namely from 5925 to 7075 cm^{-1}) in the ΓX direction and $730 \pm 32\,\mathrm{cm}^{-1}$ (namely from 5920 to 6650 cm^{-1}) in the ΓZ direction.

[52] A. Yariv and P. Yeh, in *Optical Waves in Crystals: Propagation and Control of Laser Radiation* (Wiley, New York, 1980), Chap. 6, pp. 155–219.

[53] E. Yeganegi, A. Lagendijk, A. P. Mosk, and W. L. Vos, Local density of optical states in the band gap of a finite one-dimensional photonic crystal, Phys. Rev. B **89**, 045123 (2014).

[54] C. Tserkezis, Effective parameters for periodic photonic structures of resonant elements, J. Phys.: Condens. Matter **21**, 155404 (2009).

[55] Yu. A. Vlasov, V. N. Astratov, O. Z. Karimov, A. A. Kaplyanskii, V. N. Bogomolov, and A. V. Prokofiev, Existence of a photonic pseudogap for visible light in synthetic opals, Phys. Rev. B **55**, R13357(R) (1997).

[56] J. F. Bertone, P. Jiang, K. S. Hwang, D. M. Mittleman, and V. L. Colvin, Thickness Dependence of the Optical Properties of Ordered Silica-Air and Air-Polymer Photonic Crystals, Phys. Rev. Lett. **83**, 300 (1999).

[57] N. Stefanou, C. Tserkezis, and G. Gantzounis, Plasmonic excitations in ordered assemblies of metallic nanoshells, Proc. SPIE **6989**, 698910 (2008).

[58] W. L. Vos, H. M. van Driel, M. Megens, A. F. Koenderink, and A. Imhof, Experimental probes of the optical properties of photonic crystals, in *Proceedings of the NATO ASI Photonic Crystals and Light Localization in the 21st Century*, edited by C. M. Soukoulis (Kluwer, Dordrecht, 2001), pp. 181–198.

[59] W. L. Vos, R. Sprik, A. van Blaaderen, A. Imhof, A. Lagendijk, and G. H. Wegdam, Strong effects of photonic band structures on the diffraction of colloidal crystals, Phys. Rev. B **53**, 24 (1996).

[60] H. M. van Driel and W. L. Vos, Multiple Bragg wave coupling in photonic band gap crystals, Phys. Rev. B **62**, 9872 (2000).

[61] M. A. Green, K. Emery, Y. Hishikawa, W. Warta, and E. D. Dunlop, Solar cell efficiency tables (Version 45), Prog. Photovolt. **20**, 606 (2012).

[62] A. Polman and H. A. Atwater, Photonic design principles for ultrahigh-efficiency photovoltaics, Nat. Mater. **11**, 174 (2012).

[63] D. J. Griffiths, *Introduction to Electrodynamics* (Prentice Hall, Upper Saddle River, NJ, 1999).

[64] A. Ghatak and K. Thyagarajan, *Optical Electronics* (Cambridge University Press, Cambridge, 1999).